Available online at www.sciencedirect.com
SCIENCE DIRECT®
International Journal of Heat and Mass Transfer 49 (2006) 1738–1746
International Journal of HEAT and MASS TRANSFER
www.elsevier.com/locate/ijhmt

Numerical simulation of LEC growth of InP crystal with an axial magnetic field

Mingwei Li [a,*], Chunmei Liu [b], Pingqing Wang [c]

[a] Institute of Power Engineering of Chongqing University, Chongqing 400044, China
[b] Institute of Vehicle and Motive Power Engineering of Henan University of Science and Technology, Luoyang 471003, China
[c] Bioengineering Institute of Chongqing University, Chongqing 400044, China

Received 24 June 2005; received in revised form 27 September 2005
Available online 6 December 2005

Abstract

A set of numerical analyses for momentum, heat transfer and thermal stress for a 3 in. diameter liquid encapsulant Czochralski growth of single-crystal InP with an axial magnetic field is carried out by using the finite element method. Firstly, convective and conductive heat transfers, radiative heat transfer between diffuse surfaces and the Navier–Stokes equations for both melt and encapsulant and electric current stream function equations for the melt and crystal are all combined and solved simultaneously. The thermal stress distribution in the crystal is calculated by using the obtained temperature field. The effects of some process parameters on flow, heat transfer, growing interface shape and thermal stress are investigated.

Keywords: LEC; InP; Magnetic field; Fluid flow; Heat transfer; Thermal stress

1. Introduction

Indium phosphide (InP) is an important semiconductor material in the application of optoelectronic and high frequency devices. Compared with silicon, the growth of InP is much more difficult in terms of yield and quality control. One of the methods used successfully growth of InP is the liquid-encapsulated Czochraski (LEC) technique. The LEC growth process involves various flow mechanisms. The main mechanism is natural convection in the melt due to buoyancy. Additional effects such as forced convection driven by crystal and (or) crucible rotation and Marangoni convection due to surface tension gradient also affect flow patterns in the melt. As well known, the quality of the grown crystal is associated with the melt flow. Convective transport in the melt may lead to small-scale spatial oscillations of the crystal's dopant composition, which are called striations or microsegregation and/or large-scale variations of the crystal's dopant composition, which are caused by the macrosegregation. Since molten semiconductors are excellent electrical conductors, a magnetic field can be used to control the melt motion in order to control the dopant distribution in the crystal. There have been some works that have dealt with the modeling and simulation of growth systems of InP crystal with various levels of complexity. Linear stability analysis for the buoyancy convection during the LEC growth of compound semiconductor crystals with a steady, uniform, vertical magnetic field was performed, critical Rayleigh number was obtained for the weaker and stronger magnetic fields [1]. Morton et al. [2,3] treated the species transport in an InP melt during the magnetically stabilized LEC process. Dopant distributions in the crystal and in the melt at several different stages were present for several magnetic field strengths. The effect of the convective species transport on the segregation in both the melt and the crystal was emphasized. Zhang and his coworkers [4] simulated the high pressure, liquid-encapsulated Czochraski (HPLEC) growth of InP

* Corresponding author.
E-mail address: mwlizao@yahoo.com (M. Li).

0017-9310/$ - see front matter © 2006 Elsevier Ltd. All rights reserved.
doi:10.1016/j.ijheatmasstransfer.2005.09.033

crystal, the effect of gas recirculation on melt flow and growing interface shape was studied. Their model incorporated flows induced by buoyancy and capillary forces and by crystal and crucible rotations, as well as the radiation heat loss from the melt and the crystal surface. Zou et al. [5] extended Zhang et al.'s work, calculated the thermal stress in the growing crystal and the redistribution of dopant in the melt. A 3D unsteady model including the interface shape calculation was presented in the entire LEC furnace for the first time [6]. A numerical simulation to study the batch operation of liquid-encapsulated vertical Bridgman (LEVB) crystal growth was conducted, the dynamic effects of some process parameters, including the ambient temperature distribution and the shape and anisotropic properties of the ampoule, on heat flow, the growth rate, and the growing interface shape were given [7]. Okano et al. [8] investigated the effect of crucible cap and crucible rotation on growing interface shape in vertical gradient freezing (VGF). A parallel adaptive finite element scheme was used to analyze the InP LEC melt flow, in their model only the melt phase was included [9].

In these investigations mentioned above, it should be pointed out that some of them consider the effect of magnetic field, but do not involve the movement of the growing interface and the calculation of the thermal stress in the crystal [1–3], some take the movement of the growing interface [4,6–8] and the thermal stress [5] into account but neglecting the effect of magnetic field. The present work is different from the these works, it involves not only the effect of magnetic field, but also the movement of the growing interface and the calculation of thermal stress. We perform a set of numerical simulations on momentum, heat transfer and the thermal stress for a 3 in. diameter LEC growth of single-crystal InP with an axial magnetic field by using the finite element method. The effects of the thickness of encapsulant, the imposed magnetic field strength, the crystal pulling rate as well as the crystal and crucible rotation rate on the flow, heat transfer, growing interface shape and thermal stress are discussed.

2. Model description

2.1. Physical model and basic assumptions

Schematic diagram adopted in the present analyses is shown in Fig. 1, in which the InP melt/encapsulant interface shape is calculated by solving the Young–Laplace equation. The ambient temperature T_{a1} and T_{a2} are given. The following assumptions are introduced in the model.

(1) The system is in a pseudo-steady state and is axisymmetric. (2) Both the InP melt and the boron oxide encapsulant are incompressible and the flow is laminar. (3) The magnetic Reynolds number is so small that the effect of the induced magnetic field on the applied field can be neglected. (4) The crystal behaves as a thermoelastic solid. (5) Thermophysical properties are assumed to be constant except for the dynamic viscosity of boron oxide μ. (6) No subcooling occurs at the growing interface and the interface shape coincides with the melting temperature isotherm.

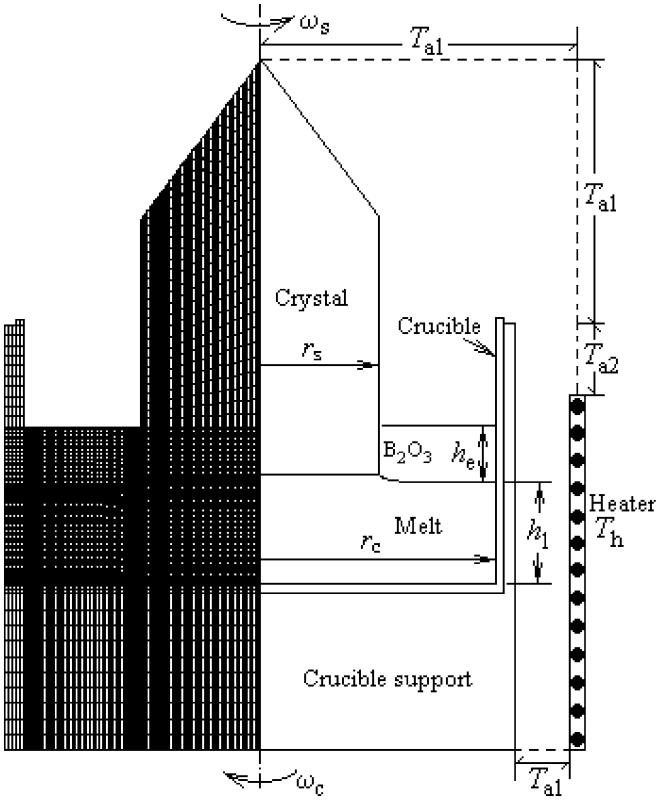

Fig. 1. Mesh (left) and schematic of model (right) for crucible (quartz), crucible support, melt, encapsulant and crystal as used to model LEC system.

2.2. Mathematical model

2.2.1. Governing equations

Under the above assumptions, the general governing equations for flow and temperature field are given by conservation equations for mass, momentum and energy as follows.

In the melt and encapsulant:

$$\nabla \cdot \mathbf{v}_i = 0, \tag{1}$$

$$\rho_i \mathbf{v}_i \cdot \nabla \mathbf{v}_i = -\nabla p_i - \nabla \cdot \boldsymbol{\tau}_i + \rho_i g \beta (T_i - T_m)\mathbf{e}_z + (J \times B), \tag{2}$$

$$\rho_i c_{pi} \mathbf{v}_i \cdot \nabla T_i = \lambda_i \nabla \cdot \nabla T_i. \tag{3}$$

In the crystal:

$$\rho_s c_{ps} V_s \mathbf{e}_z \cdot \nabla T_s = \lambda_s \nabla \cdot (\nabla T_s). \tag{4}$$

In the other solid materials:

$$\nabla \cdot (\nabla T_j) = 0, \tag{5}$$

where T, $\mathbf{v}$, p, and $\boldsymbol{\tau}$ are the temperature, velocity vector, pressure and stress tensor, respectively. T_m is the melting temperature, ρ the density, λ the thermal conductivity, β the thermal expansion coefficient, g the gravitational acceleration constant, c_p the heat capacity, V_s the crystal pulling rate, respectively. Subscripts i, s, and j indicate InP melt

($i = l$), B_2O_3 encapsulant ($i = e$), crystal and other materials, respectively. Vector $\mathbf{e}_z$ is a unit vector parallel to the z axis. Product $(J \times B)$ represents the Lorentz force due to the imposed magnetic field, in which J is the electric current density and B is strength of the magnetic field. The electric current density J is calculated by introducing the electric current stream function ψ_j which is determined by the following equation:

$$\frac{\partial}{\partial z}\left(\frac{\xi_1}{\xi}\frac{1}{r}\frac{\partial \psi_j}{\partial z}\right)+\frac{\partial}{\partial r}\left(\frac{\xi_1}{\xi}\frac{1}{r}\frac{\partial \psi_j}{\partial r}\right)=B_z\frac{\partial w}{\partial z}+B_r r\frac{\partial}{\partial z}\left(\frac{w}{r}\right), \quad (6)$$

where ψ_j is defined by

$$J_z=-\frac{\xi_1 B}{r}\frac{\partial \psi_j}{\partial r}, \quad (7)$$

$$J_r=-\frac{\xi_1 B}{r}\frac{\partial \psi_j}{\partial z}, \quad (8)$$

here ξ is the electrical conductivity, r the radius. Eq. (6) is valid in both the melt ($\xi = \xi_1$) and the crystal ($\xi = \xi_s$).

2.2.2. Boundary conditions for the temperature field

At the melt/encapsulant interface:

$$-\lambda_1 \mathbf{n}\cdot\nabla T_1=-\lambda_e \mathbf{n}\cdot\nabla T_e+q_{\mathrm{rad,l}}. \quad (9a)$$

At the encapsulant free surface:

$$-\lambda_e \mathbf{n}\cdot\nabla T_e=q_{\mathrm{rad,e}}. \quad (9b)$$

At the growing interface:

$$\lambda_1 \mathbf{n}\cdot\nabla T_1-\lambda_s n\cdot\nabla T_s=\rho_s V_s \Delta H_s \mathbf{n}\cdot e_z, \quad (9c)$$

$$T_1=T_s=T_m. \quad (9d)$$

At the encapsulated crystal side:

$$-\lambda_s \mathbf{n}\cdot\nabla T_s=-\lambda_e \mathbf{n}\cdot\nabla T_e+q_{\mathrm{rad,s}}. \quad (9e)$$

At the encapsulated crucible side:

$$-\lambda_j \mathbf{n}\cdot\nabla T_j=-\lambda_e \mathbf{n}\cdot\nabla T_e+q_{\mathrm{rad},j}. \quad (9f)$$

At the exposed crystal side and top:

$$-\lambda_s \mathbf{n}\cdot\nabla T_s=q_{\mathrm{rad,s}}. \quad (9g)$$

At the other exposed surfaces:

$$-\lambda_j \mathbf{n}\cdot\nabla T_j=q_{\mathrm{rad},j}. \quad (9h)$$

In these equations, ΔH_s is the latent heat of fusion, $\mathbf{n}$ the unit normal vector of the interface element and ε the emissivity, $q_{\mathrm{rad},i}$ is the net radiative heat flux per unit area on the surfaces, and is given by

$$q_{\mathrm{rad,i}}=\varepsilon_i\sigma_B\left[T_i^4-\left(\sum_j A_j\varepsilon_j T_j^4 G_{ji}\right)\Big/ A_i/\varepsilon_i\right], \quad (10)$$

where G_{ji} is Gebhart's absorption factor, which is the fraction of emission from surface A_j to A_i and absorbed.

2.2.3. Boundary conditions for the flow field and electric current stream function

At the side wall and the bottom of the crucible:

$$u_1=v_1=0, \quad w_1=r\omega_c, \quad \psi_j=0. \quad (11a\text{–}d)$$

At the encapsulated side wall of the crucible:

$$u_e=v_e=0, \quad w_e=r\omega_c. \quad (11e\text{–}g)$$

At the melt/encapsulant interface:

$$\mathbf{n}\cdot\mathbf{v}_1=0, \quad \mathbf{n}\cdot\mathbf{v}_e=0, \quad \psi_j=0, \quad (11h\text{–}j)$$

$$\boldsymbol{\tau}_1:\mathbf{nt}-\boldsymbol{\tau}_e:\mathbf{nt}=\gamma_{T1}\nabla T_1\cdot\mathbf{t}, \quad (11k)$$

$$\mathbf{t}\cdot\mathbf{v}_1-\mathbf{t}\cdot\mathbf{v}_e=0, \quad (11l)$$

$$\boldsymbol{\tau}_1:\mathbf{ne}_\theta-\boldsymbol{\tau}_e:\mathbf{ne}_\theta=\gamma_{T1}\nabla T_1\cdot\mathbf{e}_\theta, \quad (11m)$$

$$\mathbf{e}_\theta\cdot\mathbf{v}_1-\mathbf{e}_\theta\cdot\mathbf{v}_e=0. \quad (11n)$$

At the encapsulant surface

$$\mathbf{n}\cdot\mathbf{v}_e=0, \quad (11o)$$

$$\boldsymbol{\tau}_e:\mathbf{nt}=\gamma_{Te}\nabla T_e\cdot\mathbf{t}, \quad (11p)$$

$$\boldsymbol{\tau}_e:\mathbf{ne}_\theta=\gamma_{Te}\nabla T_e\cdot\mathbf{e}_\theta, \quad (11q)$$

At the growing interface:

$$u_1=v_1=0, \quad w_1=r\omega_s. \quad (11r\text{–}t)$$

At the encapsulated surface of the crystal:

$$u_e=v_e=0, \quad w_e=r\omega_s, \quad \psi_j=0. \quad (11u\text{–}x)$$

At the other crystal surfaces:

$$\psi_j=0. \quad (11y)$$

At the axis:

$$\psi_j=0. \quad (11z)$$

Here u, v, and w are the radial, axial and the azimuthal components of velocity, ω_s and ω_c are the angular rotation rates of the crystal and crucible, γ_{Tl} and γ_{Te} are the surface tension temperature coefficient of the melt (under B_2O_3) and surface tension temperature coefficient of boron oxide, respectively. Symbol $\mathbf{t}$ and $\mathbf{e}_\theta$ are the unit tangential and azimuthal vectors of each interface element, respectively. The growing interface shape is determined so that Eq. (9d) is satisfied, i.e., the interface coincides with the melting-point isotherm.

We define the characteristic scales of the system by T_m and ν_l/r_c for temperature and velocity, $(p - p_0 + \rho_l g z)$ for pressure, then the system is characterized by the Grashof number $Gr_l = r_c^3\beta_l T_m g/\nu_l^2$, $Gr_e = r_c^3\beta_e T_m g/\nu_l^2$, Reynolds number $Re_s = 2\pi r_c^2\omega_s/\nu_l$, $Re_c = 2\pi r_c^2\omega_c/\nu_l$, Marangoni number $Ma_1 = \gamma_{Tl} r_c T_m/\mu_l\nu_l$, $Ma_2 = \gamma_{Te} r_c T_m/\mu_l\nu_l$, Peclet number $Pe = \rho_s c_{ps} V_s r_c/\lambda_l$, Prandtl number $Pr_l = \mu_l c_{pl}/\lambda_l$, $Pr_e = \mu_e c_{pe}/\lambda_e$ and Hartmann number $Ha = r_c B/(\xi/\mu)^{1/2}$. Here μ is dynamical viscosity and ν kinematic viscosity. These non-dimension numbers are listed in Table 1. By applying Galerkin finite element method, the system gives a set of algebraic equations.

Table 1
Physical properties and processing parameters

Thermal conductivity $\lambda = 11.0$ W/m K (crystal), $\lambda = 22.0$ W/m K (melt), $\lambda = 2.0$ W/m K (B_2O_3), $\lambda = 2.98$ W/m K (quartz crucible), $\lambda = 42.0$ W/m K (crucible support)
Viscosity $\mu = 8.19 \times 10^{-4}$ kg/m s (melt), $\mu = 10^{-1.862+3650/T}$ kg/m s (B_2O_3)
Density $\rho = 4730.0$ kg/m^3 (crystal), $\rho = 5050.0$ kg/m^3 (melt), $\rho = 1648.0$ kg/m^3 (B_2O_3)
Thermal expansion coefficient $\beta = 4.44 \times 10^{-4}$ K^{-1} (melt), $\beta = 9.0 \times 10^{-5}$ K^{-1} (B_2O_3)
Surface tension temperature coefficient $\gamma_{Tl} = -1.2 \times 10^{-3}$ N/m K (between melt and B_2O_3), $\gamma_{Te} = 3.57 \times 10^{-5}$ N/m K (boron oxide free surface)
Latent heat of fusion $\Delta H_m = 735.0$ kJ/kg
Heat capacity $c_p = 170.0$ J/kg K (crystal), $c_p = 424.0$ J/kg K (melt), $c_p = 1830.0$ J/kg K (B_2O_3)
Electrical conductivity $\xi = 7.0 \times 10^5$ S/m (crystal, melt)
Emissivity $\varepsilon = 0.6$ (crystal), $\varepsilon = 0.3$ (melt), $\varepsilon = 0.65$ (B_2O_3), $\varepsilon = 0.5$ (quartz crucible), $\varepsilon = 0.9$ (crucible support)
Melting temperature $T_m = 1335$ K
Contact angle between melt and crystal $\theta_c = 45°$
Rotation rate $\omega_s = 0$–15 rpm, $\omega_c = 0$–15 rpm
Prandtl number $Pr_l = 0.0158$, $Pr_e = 915.0 \times 10^{-1.862+3650/T}$
Grashof number $Gr_l = 9.33 \times 10^{10}$, $Gr_e = 2.366 \times 10^9$
Marangoni number $Ma_1 = 9.046 \times 10^8$ (between melt and B_2O_3), $Ma_2 = -2.69 \times 10^7$ (boron oxide free surface)
Reynolds number $Re_s = 2.179 \times 10^5 \times \omega_s$, $Re_c = 2.179 \times 10^5 \times \omega_c$
Peclet number $Pe = 0.00493$–0.0196
Axial magnetic field $B = 0.456$–0.821 T
Ambient temperature $T_{a1} = 1108.0$ K, $T_{a2} = 1335.0$ K
Encapsulant thickness $h_e = 0.004$–0.04 m
Melt height $h_l = 0.035$ m
Crucible inner radius $r_c = 0.075$ m
Crystal radius $r_s = 0.0375$ m

In the present work, the diameter and length of the crystal and the heater temperature are given. The crystal pull rate is determined as one of the unknown variables, together with velocities, pressures, temperatures, electric current stream function and the growing interface coordinates, by simultaneously solving the set of nonlinear algebraic equations using Newton–Raphson method. The radiative heat exchange in the semi-transparent boric oxide layer is calculated by using the band-energy method [10]. The total number of elements, nodal points and unknowns are 9127, 9343 and 40 829, respectively. The sizes of the minimum elements in the melt are $\Delta r_{min} = 0.1774$ mm, $\Delta z_{min} = 0.68$ mm. No obvious change in accuracy is found for the further fine mesh. Typical conditions are listed in Table 1, together with the thermophysical properties used in this work. Due to lack of the surface tension temperature coefficient of InP (under B_2O_3), the value of GaAs is applied to the present calculation. Numerical procedure used here is identical to our previous paper [11,12]. The thermal-elastic stress calculation is performed after the temperature distribution in the crystal has been obtained. The calculation assumes that surface forces vanish on the surface of the crystal.

3. Results

A series of simulations under different operating conditions has been conducted. The effects of the thickness of encapsulant, imposed magnetic field strength, and the crystal pulling rate, as well as the crystal and crucible rotation rate on the flow, heat transfer, growing interface shape and thermal stress are discussed in the following subsections.

3.1. Effect of encapsulant thickness

Fig. 2a–c and Table 2 present the effects of the thickness of encapsulant, h_e, on the flow, heat transfer, thermal stress and the growing interface shape for a fixed Hartmann number ($Ha = 1400$) and a pulling rate ($V_s = 6.45$ mm/h) in the absence of the crystal and crucible rotation. The melt flow driven by the buoyancy force combined with the thermocapillary force is characterized by a counterclockwise circulation flow, which is confined in the outer core region below the melt/encapsulant interface. The melt in the inner core region below the growing interface is almost stagnant as shown in Fig. 2a and b. Hartmann layer caused by strong magnetic field is observed adjacent to the crucible's vertical wall, which agrees qualitatively with the asymptotic solution [3]. The maximum velocity V_{max} and the average velocity V_{av} decreases slightly from 0.094 cm/s to 0.083 cm/s and 0.025 cm/s to 0.022 cm/s, respectively, when increasing the thickness of encapsulant from $h_e = 0.2$ cm to 4.0 cm as indicated in Table 2. In the thin encapsulant of $h_e = 0.2$ cm, a clockwise circulation flow induced by thermocapillary force can be found (see Fig. 2a). When thickening the encapsulant to $h_e = 4.0$ cm, a bigger buoyancy force driven cell appears, it occupies upper part of the encapsulant layer, in this case the thermocapillary force driven cell still exists just above the melt/encapsulant interface due to the melt/encapsulant interface drag (see Fig. 2b). Because B_2O_3 encapsulant inhibits the radiation heat loss from the crystal surface, the total heat flow across the growing interface, Q_s, decreases from 114.4 W to 102.9 W as h_e increases from 0.2 cm to 4.0 cm. Correspondingly, the needed heater temperature decrease to

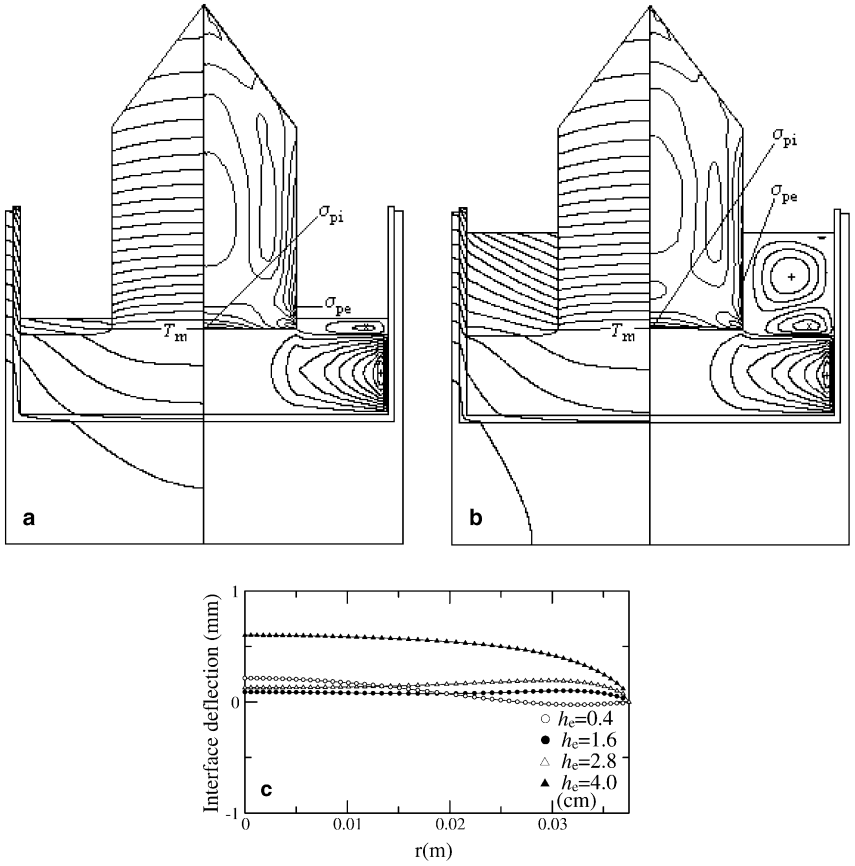

Fig. 2. Effect of encapsulant thickness. Isotherms separated by steps of 10 K (left shown in a and b), contours of stream function separated by 5×10^{-8} m^3/s (for melt) and 2.5×10^{-9} (for encapsulant) (right in the melt and encapsulant shown in a and b), contours of Von Mises stress separated by 4.5 MPa (right in the crystal shown in a and b) and interface deflection under the conditions of $Ha = 1400$, $V_s = 6.45$ mm/h, $\omega_s = \omega_f = 0$ rpm. (a) $h_e = 0.4$ cm, (b) $h_e = 4.0$ cm, (c) interface deflection for several different h_e.

1406.2 K, 6 K lower than that of $T_h = 1412.4$ for thin encapsulant as listed in Table 2. The growing interface shapes for various thickness of the encapsulant are shown in Fig. 2c. Relatively speaking, the interface deflection is not very big, the maximum deflection of the interface, D_{max}, is 0.6 mm in the case of $h_e = 4.0$ cm (see Table 2). However, there exists an obvious difference of the growing interface shape under various thickness of encapsulant. Let us divide the growing interface into two portions: the central portion ($r = 0$–0.02 m) and outer portion ($r = 0.02$–0.0375 m). For the thicker encapsulant, the whole interface shape is concave (concave to the melt) due to the effective heat exchange on the crystal surface by stronger convective in the encapsulant. However, for the thin one ($h_e = 0.2$ cm), a concave interface at the central portion and a convex interface at the outer portion are observed, this means that the heat transfer path at the periphery is from the encapsulant to the crystal. As mentioned above, Q_s is the total heat flow crossing the growing interface and it is larger in the case of $h_e = 0.2$ cm, ($Q_s = 114.4$ W), this implies that more heat need to be carried away from the central portion of the growing interface. This results in a bigger temperature gradient in the center of the growing interface for the situation of thin encapsulant, which is the origin of the larger Von Mises stress. From the contours of the Von Mises stress given in the right half part of the crystal (see Fig. 2a and b), the stress distributions look similar, but with different magnitude. There exist two peak stress spots, σ_{pi} and σ_{pe}, one locates at the center of growing interface (σ_{pi}), and another one occurres at the edge of crystal just above the encapsulant surface (σ_{pe}). The peak stresses σ_{pi} and σ_{pe} change from 41.3 MPa to 34.0 MPa and from 39.1 MPa to 30.7 MPa with the increase of the thickness of the encapsulant from $h_e = 0.2$ cm to $h_e = 4.0$ cm, respectively, (see Table 2). Obviously, $\sigma_{pi} > \sigma_{pe}$, the maximum Von Mises stress appears at the center of the growing interface.

3.2. Effect of magnetic field strength

In the present calculation, a proper magnetic field strength should be imposed in order that the laminar flow assumption can hold. Magnetic field strength between 0.456 T and 0.821 T ($Ha = 1000$–1800) is demonstrated appropriate for the convergence of the calculation. From the contours of stream function in the melt and in the encapsulant shown in Fig. 3a and b, one can see that

Table 2
Heater temperature and some representative values of the simulation results under different operating conditions

		T_h (K)	V_{max} (cm/s)	V_{av} (cm/s)	Q_s (W)	D_{max} (mm)	σ_{pi} (MPa)	σ_{pe} (MPa)
Case I: h_e (cm) ($\omega_s = \omega_c = 0$ rpm,	0.4	1412.4	0.094	0.025	114.4	0.214	41.3	39.1
$Ha = 1400$, $V_s = 6.45$ mm/h)	1.6	1409.2	0.088	0.024	109.3	0.089	37.8	32.8
	2.8	1407.3	0.084	0.023	104.2	0.192	35.05	30.3
	4.0	1406.2	0.083	0.022	102.9	0.601	34.0	30.7
Case II: Ha ($h_e = 1.6$ cm,	1000	1407.9	0.176	0.053	104.9	−1.737	30.1	31.0
$\omega_s = \omega_c = 0$ rpm, $V_s = 6.45$ mm/h)	1200	1409.1	0.124	0.034	107.6	−0.577	34.8	32.1
	1600	1409.0	0.066	0.017	110.4	0.464	39.66	33.3
	1800	1408.8	0.051	0.013	111.0	0.69	40.8	33.6
Case III: V_s (mm/h) ($h_e = 1.6$ cm,	3.23	1411.8	0.091	0.026	106.4	−1.197	32.0	31.4
$Ha = 1400$, $\omega_s = \omega_c = 0$ rpm)	6.45	1409.2	0.088	0.024	109.3	0.089	37.8	32.8
	9.67	1406.6	0.086	0.021	112.3	1.4	44.2	34.3
	12.9	1403.9	0.083	0.019	115.2	2.74	51.3	35.8
Case IV: ω_s (rpm) ($h_e = 1.6$ cm,	1	1409.2	0.095	0.024	109.3	0.0873	37.8	32.8
$Ha = 1400$, $\omega_c = 5$ rpm, $V_s = 6.45$ mm/h)	5	1409.3	0.095	0.023	109.5	0.162	38.1	32.9
	10	1409.4	0.095	0.024	110.0	0.4	39.0	33.1
	15	1409.5	0.169	0.028	110.8	0.753	40.4	33.4
Case V: ω_c (rpm) ($h_e = 1.6$ cm,	1	1409.3	0.088	0.023	109.5	0.17	38.1	32.9
$Ha = 1400$, $\omega_s = 5$ rpm, $V_s = 6.45$ mm/h)	10	1409.3	0.116	0.024	109.4	0.14	37.9	32.8
	15	1409.3	0.34	0.025	109.3	0.128	37.7	32.8

V_{max} maximum velocity in the melt; V_{av} average velocity in the melt defined as $V_{av} = \sum \left(\sqrt{u_i^2 + v_i^2}\right)/N$, here N represents the total number of the nodes in the melt; Q_s total heat flow across the growing interface; D_{max} maximum deflection of growing interface. The symbol minus "−" means that the interface is convex (to the melt); σ_{pi} peak of thermal stress at the growing interface; σ_{pe} peak stress at the edge of crystal just above the encapsulant surface.

the contours of stream function are more dense for the smaller Hartmann number than that for the larger one. This implies that the reduction effect of the axial magnetic field on the flow is significant. The reduction effect can also be found from the change of the maximum velocity V_{max} from 0.176 cm/s to 0.051 cm/s and the change of average velocity V_{av} from 0.053 cm/s to 0.013 cm/s as increase the magnetic field strength from $Ha = 1000$ to $Ha = 1800$, respectively, as listed in Table 2. Interestingly, the stronger melt flow with the smaller Ha is still maintained in the outer core region below the melt/encapsulant interface, does not penetrate into the inner core region below the growing interface. This flow feature combined with the stronger encapsulant flow makes the heat transport crossing melt/encapsulant interface and consequently passing the encapsulant layer much effective, so that the total heat flow crossing the growing interface (Q_s) decreases. As a result, the interface shape becomes more convex (to the melt) with $Ha = 1000$. On the contrast for the stronger magnetic field, more heat flow passing the growing interface, so the interface is slightly concave to the melt (see Fig. 3c). The peak values of the stress at the growing interface σ_{pi} and at the edge of crystal σ_{pe} increase from 30.1 MPa to 40.8 MPa and from 31.0 MPa to 33.6 MPa as Hartmann number changes from $Ha = 1000$ to $Ha = 1800$, respectively. Comparing the two peak values σ_{pi} and σ_{pe}, it is clear that the maximum Von Mises stress locates at the growing interface for most of Hartmann number except for the case of $Ha = 1000$, in which case the maximum Von Mises stress appears at the edge of the crystal just above the encapsulant.

3.3. Effect of crystal pulling rate

Due to the space limitation, here we do not represent the isotherms and contours of stream function and Von Mises stress but give some representative values as listed in Table 2 and the interface shapes as shown in Fig. 4. As a higher pulling rate is associated with a more release of the latent heat, so with the increase of pulling rate, the heater temperature needed should be cut down properly. Meanwhile, it should be emphasized that the solidification heat generated at the growing interface must be carried away mainly by the crystal, as pointed out by Lan [7] that higher axial thermal gradients could remove the heat of fusion away more effectively, and thus result in a less concave interface, so in the present situation, the growing interface shape convents from convex to concave with increasing the pulling rate (see Fig. 4). The maximum deflection of interface reaches to 2.74 mm in the case of $V_s = 12.9$ mm/h. There exist no noticeable difference in the melt flow pattern with rising the pulling rate, but the maximum velocity V_{max} and the average velocity V_{av} in the melt decreases from 0.091 cm/s to 0.083 cm/s and from 0.026 cm/s to 0.019 cm/s, respectively, as shown in Table 2. The maximum Von Mises stress appears in the center of the growing interface for various pulling rates. Specially, maximum Von Mises stress increases by 60% as enhancing the pulling rate from 3.23 mm/h to 12.9 mm/h.

3.4. Effect of crystal and crucible rotation

With increasing rotation rate of crystal to $\omega_s = 15$ rpm, a new cell appear underneath the growing interface near

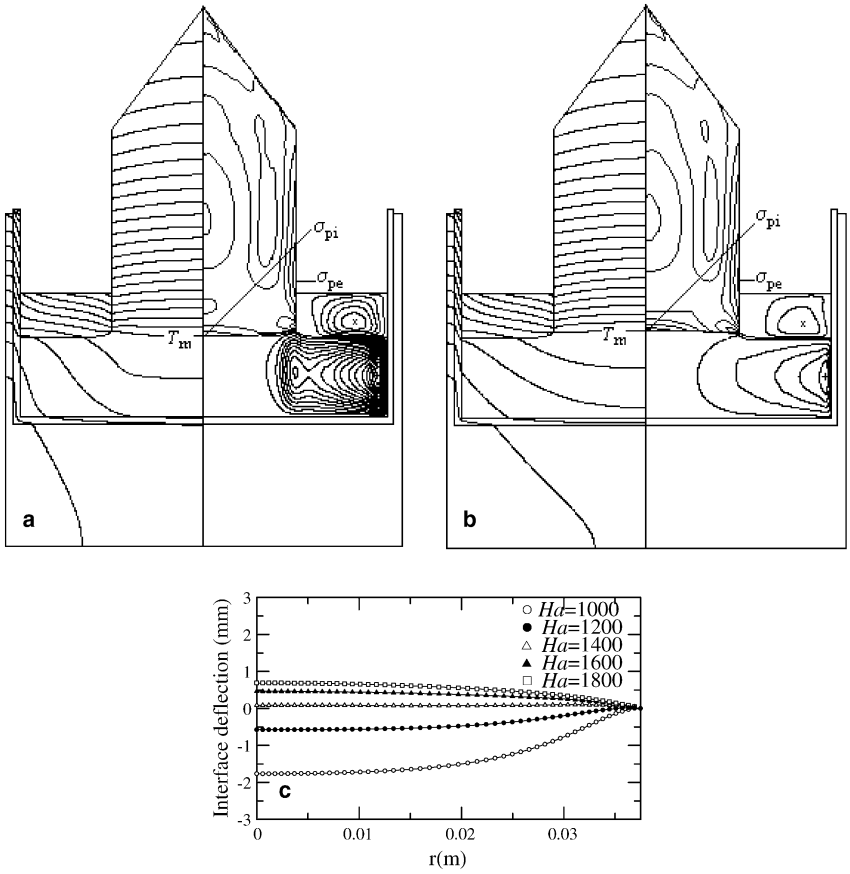

Fig. 3. Effect of magnetic field strength. Isotherms separated by steps of 10 K (left shown in a and b), contours of stream function separated by 5×10^{-8} m^3/s (for melt) and 2.5×10^{-9} (for encapsulant) (right in the melt and encapsulant shown in a and b), contours of Von Mises stress separated by 4.5 MPa (right in the crystal shown in a and b) and interface deflection under the conditions of $h_e = 1.6$ cm, $V_s = 6.45$ mm/h, $\omega_s = \omega_f = 0$ rpm. (a) $Ha = 1000$, (b) $Ha = 1800$, (c) interface deflection for several different Ha.

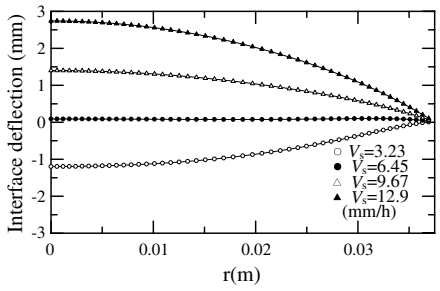

Fig. 4. Interface deflection under the conditions of $h_e = 1.6$ cm, $Ha = 1400$, $\omega_c = \omega_c = 0$ rpm for several different pulling rate V_s.

closely the periphery as demonstrated in Fig. 5a. Particularly, one can see that the slender meridional flow cell breaks into two cells and the maximum velocity V_{max} becomes rather large in this case. It is not difficult to see from Fig. 5b and Table 2 that the growing interface becomes more concave and the thermal stress increases slightly with the enhancement of the crystal rotation rate. Besides, the effect of the crystal rotation rate on the heater temperature T_h is insignificant. Except the maximum velocity increases largely, the influence of the crucible rotation on the flow, heat transfer, interface shape and thermal stress is negligible (see Table 2).

As the heat flow crossing the growing interface is connected to the axial gradient, and the elastic stress is linearly proportional to the gradient, so from the data listed in Table 2 we note that the maximum value of the thermal stress (σ_{pi}) is linearly proportional to the total heat flow from the growing interface (Q_s). Meanwhile the maximum value of the Von Mises stress gets larger in the case where the interface become more concave to the melt, this is consistent qualitatively with the result of Ref. [5].

The typical maximum value of the Von Mises stress for LEC-crystals is 25 MPa as pointed out by Sahr et al. [13], the maximum value of the Von Mises stress obtained in the present calculation are larger than this value and slightly larger than those given by Zou et al. [5] and Sahr et al. [13], so it is very dangerous and the dislocation maybe generate at the growing interface. Compared with the available experiment result [14], the calculated interface deflection in the present work is notably smaller, this maybe originate from the unrealistic ambient conditions adopted in present work, such as neglecting the gas flow.

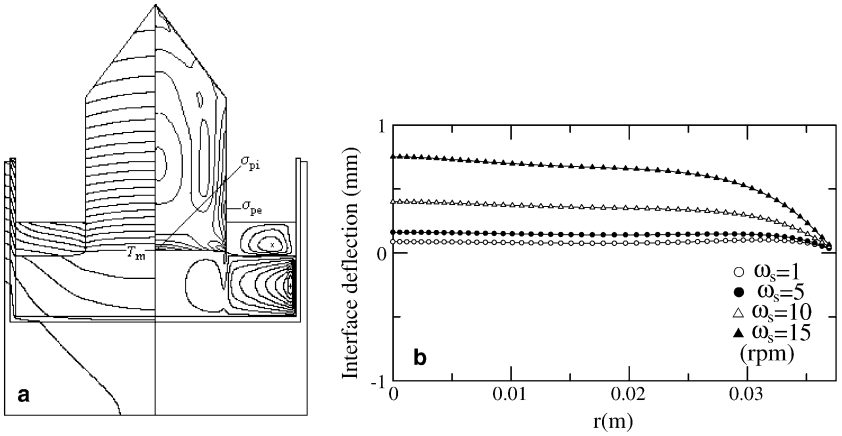

Fig. 5. Effect of crystal rotation. Isotherms separated by steps of 10 K (left shown in a), contours of stream function separated by 5×10^{-8} m^3/s (for melt) and 2.5×10^{-9} (for encapsulant) (right in the melt and encapsulant shown in a), contours of Von Mises stress separated by 4.5 MPa (right in the crystal shown in a) and interface deflection under the conditions of $h_e = 1.6$ cm, $V_s = 6.45$ mm/h, $Ha = 1400$, $\omega_c = 5$ rpm. (a) $\omega_s = 15$, (b) interface deflection for several different ω_s.

4. Conclusions

A global simulation code was applied to numerically study the characteristics of flow, heat transfer and the thermal stress in LEC growth of InP with an axial magnetic field. The results indicate that:

1. The encapsulant thickness changes the conditions of the radiation and convective heat transfer on the crystal surface, this results in a dramatically change of the interface shape, which is associated with the thermal stress. But, relatively speaking, the effect of the encapsulant thickness on the interface deflection is small.
2. With increasing the magnetic field strength, the flow in both the melt and the encapsulant decreases, more heat flow passes through the growing interface. As a consequence, the interface shape changes from convex to concave (to the melt). Higher thermal stress is observed in the case of stronger magnetic field strength.
3. The influence of the pulling rate on the interface shape is relatively larger. The maximum deflection of interface reaches to 2.74 mm in the case of $V_s = 12.9$ mm/h. With enhancing the pulling rate, the interface shape convents from convex to concave, and the maximum Von Mises stress increases rather remarkably.
4. The flow pattern may be influenced by the rotation rate of the crystal. Multi-cell flow pattern may appear in the melt with large crystal rotation rate. However, totally speaking, the effect of the crystal and the crucible rotation on the flow and heat transfer as well as the thermal stress is not so obvious, except the maximum velocity in the melt.

Gas convection is important mechanism for heat transfer to the grown crystal [4], it is therefore important to conduct a more efficient numerical simulation involving calculating three-dimension turbulent flow in the melt and in the gas phase for a more realistic ambient conditions in the future.

Acknowledgement

This work was supported by NSFC with Grant No. 50376078, by the Excellent Young Teachers Program of MOE (EYTP), P.R.C., [2002]40, and by Second-Term National 985 Project within Research Center of Biological Function Information and Instruments of Chongqing University.

References

[1] J.S. Walker, D. Henry, H. BenHadid, Magnetic stabilization of the buoyant convection in the liquid encapsulated Czochralski process, J. Cryst. Growth 243 (2002) 108–116.
[2] J.L. Morton, N. Ma, D.F. Bliss, George G. Bryant, Dopant segregation during liquid encapsulated Czochralski crystal growth in a steady axial magnetic field, J. Cryst. Growth 242 (2002) 471–485.
[3] J.L. Morton, N. Ma, D.F. Bliss, George G. Bryant, Magnetic field effects during liquid encapsulated Czochralski growth of doped photonic semiconductor crystals, J. Cryst. Growth 250 (2003) 174–182.
[4] H. Zhang, V. Prasad, D.F. Bliss, Modeling of high pressure, liquid-encapsulated Czochraski growth of InP crystal, J. Cryst. Growth 169 (1996) 250–260.
[5] Y.F. Zou, G.-X. Wang, H. Zhang, V. Prasad, D.F. Bliss, Macro-segregation, dynamics of interface and stresses in high pressure LEC grown crystal, J. Cryst. Growth 180 (1997) 524–533.
[6] E.N. Bystrova, V.V. Kalaev, O.V. Smirnova, E.V. Yakovlev, Yu.N. Makarov, Prediction of the melt/crystal interface shape geometry in liquid encapsulated Czochralski growth of InP bulk crystals, J. Cryst. Growth 250 (2003) 189–194.
[7] C.W. Lan, C.C. Ting, Numerical investigation on the batch characteristics of liquid encapsulated vertical Bridgman crystal growth, J. Cryst. Growth 149 (1995) 175–186.
[8] Y. Okano, H. Kondo, S. Dost, Numerical study of interface shape control in the VGF growth of compound semiconductor crystal, J. Cryst. Growth 237–239 (2002) 1769–1772.

[9] D. Givoli, J.E. Flaherty, M.S. Shephard, Analysis of InP LEC melt flows using a parallel adaptive finite element scheme, J. Cryst. Growth 180 (1997) 510–516.
[10] F. Dupret, P. Nicodeme, Y. Ryckmans, P. Wouters, M.J. Crochet, Global modeling of heat transfer in crystal growth furnaces, Int. J. Heat Mass Transfer 33 (9) (1990) 1849–1871.
[11] M.W. Li, Y.R. Li, N. Imaishi, T. Tsukada, Global simulation of a silicon Czochralski furnace, J. Cryst. Growth 234 (2002) 32–46.
[12] M.W. Li, W.R. Hu, N.H. Chen, D.L. Zeng, Z.M. Tang, Numerical analysis of LEC growth of GaAs with an axial magnetic field, Int. J. Heat Mass Transfer 45 (2002) 2843–2851.
[13] U. Sahr, G. Müller, Growth of InP substrate crystals by the vertical gradient freeze technique, in: Conference Proceedings of 12th Semiconducting and Insulating Materials Conference, 2002, pp.13–18.
[14] K. Kohir, M. Ohta, O. Oda, Growth of long-length 3 inch diameter Fe-doped InP single crystals, J. Cryst. Growth 158 (1996) 197–204.